Research article

Vlastimil Křápek*, Andrea Konečná, Michal Horák, Filip Ligmajer, Michael Stöger-Pollach, Martin Hrtoň, Jiří Babocký and Tomáš Šikola

Independent engineering of individual plasmon modes in plasmonic dimers with conductive and capacitive coupling

https://doi.org/10.1515/nanoph-2019-0326
Received August 23, 2019; revised October 29, 2019; accepted November 11, 2019

Abstract: We revisit plasmon modes in nanoparticle dimers with conductive or insulating junction resulting in conductive or capacitive coupling. In our study, which combines electron energy loss spectroscopy, optical spectroscopy, and numerical simulations, we show the coexistence of strongly and weakly hybridised modes. While the properties of the former ones strongly depend on the nature of the junction, the properties of the latter ones are nearly unaffected. This opens up a prospect for independent engineering of individual plasmon modes in a single plasmonic antenna. In addition, we show that Babinet's principle allows to engineer the near field of plasmon modes independent of their energy. Finally, we demonstrate that combined electron energy loss imaging of a plasmonic antenna and its Babinet-complementary counterpart allows to reconstruct the distribution of both electric and magnetic near fields of localised plasmon resonances supported by the antenna, as well as charge and current antinodes of related charge oscillations.

Keywords: plasmonics; localised surface plasmons; electron energy loss spectroscopy; Babinet's principle; hot spot.

1 Introduction

Plasmonic antennas are metallic particles widely studied for their ability to control, enhance, and concentrate the electromagnetic field [1]. Strikingly, the field in the vicinity of the plasmonic antennas, the so-called near field, can be confined into a deeply subwavelength region, where it is enhanced with respect to the driving field. This effect stems from the excitation of localised surface plasmons (LSPs) – quantised oscillations of the free electron gas in the metal coupled to the evanescent electromagnetic waves. Plasmonic antennas are promising for applications such as energy harvesting, nonlinear optics [2, 3], sensing [4], enhanced emission [5], or as building blocks of metasurfaces [6].

Properties of LSP can be engineered by adjusting the shape, size, and composition of the plasmonic antennas, by changing their dielectric environment, or by composing single antennas into more complex structures – dimers and multimers. Localised surface plasmon modes in the dimers can be described in terms of hybridisation [7, 8]: the modes of individual antennas combine into bonding and antibonding hybridised modes. For large enough separation between the components of the dimer antenna, the coupling between the modes can be described as a dipole–dipole coupling [7]. For closely spaced components, more complex hybridisation models exist involving multipolar terms [9] or near-field coupling [8]. Instead of this capacitive

***Corresponding author: Vlastimil Křápek,** Central European Institute of Technology, Brno University of Technology, Purkyňova 123, 612 00 Brno, Czech Republic; and Institute of Physical Engineering, Brno University of Technology, Technická 2, 616 69 Brno, Czech Republic, e-mail: vlastimil.krapek@ceitec.vutbr.cz. https://orcid.org/0000-0002-4047-8653
Andrea Konečná: Theory of Nanophotonics, Materials Physics Center CSIC-UPV/EHU, Paseo Manuel de Lardizabal 5, 20018 San Sebastián, Spain. https://orcid.org/0000-0002-7423-5481
Michal Horák, Filip Ligmajer, Martin Hrtoň and Jiří Babocký: Central European Institute of Technology, Brno University of Technology, Purkyňova 123, 612 00 Brno, Czech Republic. https://orcid.org/0000-0001-6503-8294 (M. Horák); https://orcid.org/0000-0003-0346-4110 (F. Ligmajer); https://orcid.org/0000-0002-3264-4025 (M. Hrtoň)
Michael Stöger-Pollach: University Service Centre for Transmission Electron Microscopy, Vienna University of Technology, Wiedner Hauptstraße 8-10, A-1040 Wien, Austria. https://orcid.org/0000-0002-5450-4621
Tomáš Šikola: Central European Institute of Technology, Brno University of Technology, Purkyňova 123, 612 00 Brno, Czech Republic; and Institute of Physical Engineering, Brno University of Technology, Technická 2, 616 69 Brno, Czech Republic. https://orcid.org/0000-0003-4217-2276

coupling, the components can be coupled conductively by a metallic junction. The effects of the transformation between the capacitive and conductive coupling have been thoroughly studied [10, 11], indicating pronounced qualitative and quantitative changes in the properties of LSP modes, going far beyond the simple hybridisation concept in the case of a conductive coupling.

Babinet's principle represents another concept for engineering LSP modes. It relates optical response of thin solid and hollow antennas: metallic particles and apertures in the metallic films of the same size and shape. Both types of antennas provide complementary response with identical energies of LSP modes but with interchanged electric and magnetic field [12–15]. Applicability of Babinet's principle in plasmonics over a broad spectral range from THz to visible has been experimentally demonstrated [16–19] with quantitative deviations being observed, in particular at optical frequencies [18, 20]. Babinet's principle has been used to design plasmonic structures with advanced functionalities including metasurfaces and metamaterials [13, 21] or antennas with electromagnetic hot spots [22]. It is also used as a tool for indirect imaging of magnetic field. Here, the magnetic field distribution formed by a planar object of interest is first related through Babinet's principle to the electric field distribution for a complementary structure (interchanging conducting and insulating parts), which is considerably easier to detect. The electric field distribution is then retrieved by one of available methods such as the electron energy loss spectroscopy (EELS) [17, 19, 20, 23, 24] or near-field microscopy [16]. Babinet's reciprocity between electric and magnetic field has been also used to interchange electric and magnetic hot spots [22].

Several interesting phenomena and applications of plasmonic antennas involve more than one LSP mode. For example, photoluminescence enhancement requires enhancement at the energies of the excitation and emission and also suppressed coupling of the emitter to nonradiative LSP modes, which quench the emission [25]. Directional scattering is realised through the interference of the fundamental and excited LSP modes [26]. Metasurfaces with high transmission efficiency based on Huygens meta-atoms [27] utilise Kerker effect [28, 29] based on the spectral overlap of electric and magnetic plasmon modes. Interference of bright and dark LSP modes results into Fano resonances [30] related to plasmon-induced transparency [31] or sensing [32]. It is thus desirable to have a tool for independent engineering of individual plasmon modes in a single antenna.

Here we present such a tool. We show that by switching between the capacitive and conductive coupling in bowtie antennas, the properties of some LSP modes are changed pronouncedly, whereas other modes are almost unaffected. We also show that by employing Babinet's principle it is possible to modify the near field of LSP modes while preserving their energy. This demonstrates feasibility of individual engineering of LSP modes in single plasmonic antennas.

2 Methods

2.1 Fabrication of antennas

Plasmonic antennas for EELS measurement were fabricated by focused ion beam (FIB) lithography. First, we deposited 30-nm-thick gold layer on 30-nm-thick standard silicon nitride membrane for transmission electron microscopy (TEM) with the window size of 250×250 μm^2 (Agar Scientific). Gold layer was deposited without any adhesion layer by ion beam–assisted deposition. Second, we performed FIB lithography in dual-beam FIB/SEM microscope FEI Helios using gallium ions with the energy of 30 keV and ion beam current of 2.6 pA. We note that the energy (the highest available) and the current (the lowest available) are optimised for the best spatial resolution of the milling. Direct antennas were situated in the middle of a metal-free square (between 2×2 and 4×4 μm^2), which is perfectly sufficient to prevent their interaction with the surrounding metallic frame [33]. Inverted antennas were fabricated as isolated antennas with the distance between two nearby structures at least of 5 μm to prevent their collective interaction.

Plasmonic antennas for optical measurement were fabricated by electron beam lithography (EBL). We note that a good correspondence between the properties of antennas fabricated by EBL and FIB has been established [34]. Our choice of the method is guided by the ease of fabrication of antennas on TEM membranes for EELS (FIB) and on thick substrates for optical measurements (EBL).

2.2 Electron energy loss spectroscopy

Electron energy loss spectroscopy measurements were performed with TEM FEI Titan equipped with GIF Quantum spectrometer operated in monochromated scanning regime at 300 kV. Beam current was set to 0.4 nA, and the full width at half maximum of the zero-loss peak was around 0.1 eV. We set convergence angle to 10 mrad,

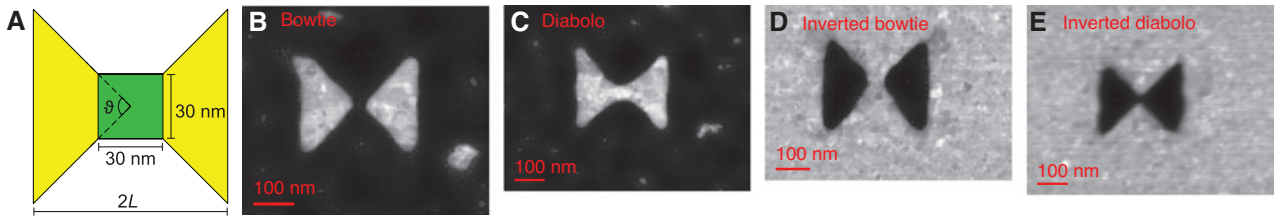

Figure 1: Bowtie and diabolo plasmonic antennas.
(A) Schematic representation of the bowtie and diabolo antennas: wings (yellow), bridge (green). *L* denotes the length of the wing. (B–E) High-angle annular dark field (HAADF) images of (B) bowtie, (C) diabolo, (D) inverted bowtie, and (E) inverted diabolo antennas. Bright/dark colour corresponds to gold/substrate, respectively.

collection angle to 10.4 mrad, and dispersion of the spectrometer to 0.01 eV/pixel. We recorded electron energy loss (EEL) spectrum images with the pixel size of 5 nm, while the number of pixels depended on the antenna size. Every pixel consists of 30 cross-correlated EEL spectra with the acquisition time around 25 s for each spectrum. EEL spectra were integrated over several pixels around the positions of interest, background, and zero-loss peak subtracted and divided by the integral intensity of the whole spectrum to transform measured counts to a quantity proportional to the loss probability. EEL maps were obtained as energy-integrated intensity at the plasmon peak energy with the energy window of 0.1 eV divided pixel-by-pixel by the integral intensity of the zero-loss peak (integration window from −0.5 to 0.5 eV).

The relation of the measured loss probability to the near field of LSP modes is as follows. The probing electron transfers a part of its energy $\hbar\omega$ to an LSP mode in the specimen with the probability density (so-called loss probability) $\Gamma(\omega)$ reading [35]

$$\Gamma(\omega)=\frac{e}{\pi\hbar\omega}\int dt\,\mathrm{Re}\{\exp(-i\omega t)\mathbf{v}\cdot\mathbf{E}^{\mathrm{ind}}[\mathbf{r}_e(t),\omega]\}$$

where $\mathbf{E}^{\mathrm{ind}}[\mathbf{r}_e(t),\omega]$ is the field induced by the electron moving with the velocity $\mathbf{v}$ at the position of the electron $\mathbf{r}_e(t)$. For the electron with the trajectory perpendicular to the sample (along the axis z), it is an out-of-plane component of the field (E_z) that is relevant for the interaction. Correspondence between the loss probability and the electromagnetic local density of states projected along the electron beam trajectory has been thoroughly discussed [36–38].

2.3 Optical measurements

The far-field extinction $(1-T/T_{\mathrm{ref}})$ spectra were acquired using an infrared microscope [Bruker Hyperion 3000 (Ettlingen, Germany), 36× objective, NA = 0.5] coupled to a Fourier-transform infrared spectrometer (Bruker Vertex 80V). Each spectrum was referenced to a bare substrate in the vicinity of the respective antenna array.

2.4 Simulations

In all simulations, the bowtie and diabolo antennas have been represented by two gold triangles or triangular apertures (as shown in Figure 1) of a height of 30 nm on top of 30-nm-thick silicon nitride membrane. The dielectric function of gold was taken from [39], and the dielectric constant of the silicon nitride membrane was set equal to 4, which is a standard approximation in the considered spectral region [40].

EEL spectra have been calculated with finite element method using a commercial software COMSOL Multiphysics (Burlington, MA, USA).

3 Results and discussion

Plasmonic antennas of four different types – bowtie, diabolo, inverted bowtie, and inverted diabolo – have been fabricated by FIB lithography or EBL (see Methods for details) and characterised by EELS, transmission spectroscopy, and electromagnetic simulations.

Figure 1A shows the design of the bowtie and diabolo plasmonic antennas. They consist of wings (metallic for the bowtie and diabolo) and a bridge, which is insulating for a bowtie (referred to as the gap in such a case) and metallic for a diabolo. For inverted structures, metallic and insulating parts are interchanged. The dimensions of the bridge are set to 30 × 30 nm, and the wing length L is varied. The wing angle ϑ is set to 90°, which results into 1:1 rate of metal and insulator in the active zone of the antennas and ensures maximum complementarity of direct and inverted antennas. Bowtie and inverted diabolo antennas concentrate charge and form electric hot spots (areas of

high field concentration), while diabolo and inverted bowtie antennas funnel current and form magnetic hot spots [22]. Typical fabricated antennas are shown in Figure 1B–E. Their clearly visible polycrystalline character shall not have profound influence on the plasmonic properties, as shown by former studies [11].

First, we will discuss plasmonic properties of bowtie antennas. Typical bowtie with the wing size of 141 ± 5 nm is shown in Figure 2A. EEL spectra recorded at different positions reveal three distinct peaks at the energies of 1.22, 1.67, and 1.95 eV, as observed in Figure 2B. Experimental spectra are reasonably well reproduced with calculations (Figure 2C). The nature of the peaks is revealed in the energy-filtered maps of the loss intensity. The loss intensity is related to the plasmon electric field parallel with the trajectory of the electron beam E_z [35], which is the largest at the charge antinodes (current nodes) of plasmon oscillations. Further insight is provided by the calculated induced field and charge distributions (see Supporting Information, Sec. S3, for calculated maps of the electric field and charge and a detailed discussion). Due to large wing angle (90°), the lowest peak at 1.22 eV corresponds to the transverse dipolar (TD) modes with the charge oscillating in the direction perpendicular to the antenna's long axis. The interaction between the oscillating dipoles in both wings gives rise to two hybridised modes: the transverse dipolar bonding (TDB) and transverse dipolar antibonding (TDA) [7, 10]. The modes cannot be resolved in the experiment. In the simulations, the TDA mode is featured as a weak high-energy shoulder of the

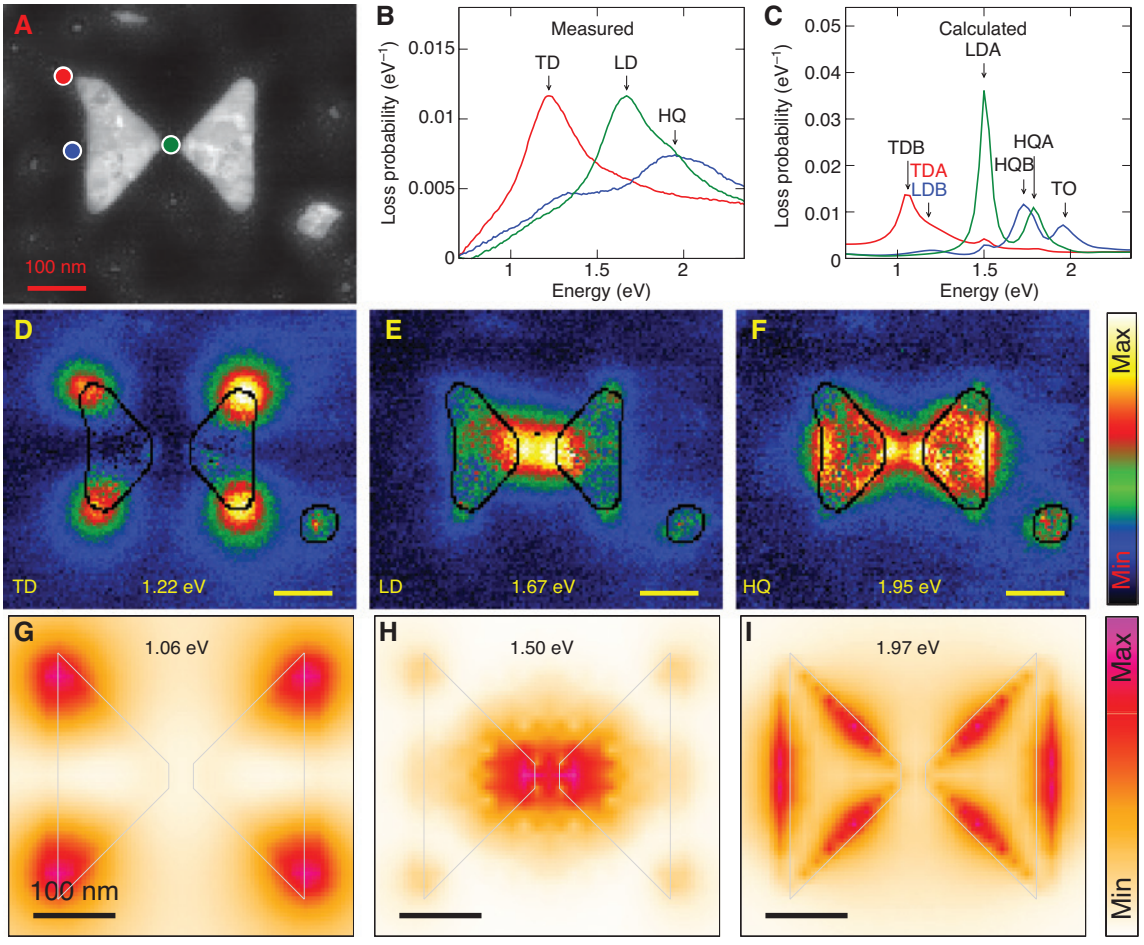

Figure 2: Bowtie antenna with the wing length $L = 141$ nm.
(A) HAADF image. (B, C) EEL spectra recorded at specific points indicated by colour spots in panel A (the spectrum displayed by a specific colour corresponds to the spot of the same colour): (B) measured, (C) calculated. The labels of the peaks and modes are explained in the text. (D–F) Experimental energy-filtered maps of the loss intensity for (D) transverse dipolar mode (TD, $E = 1.22$ eV), (E) longitudinal dipolar mode (LD, $E = 1.67$ eV), (F) hexapolar–quadrupolar mode (HQ, $E = 1.95$ eV). (G–I) Calculated loss intensity maps at the energy of (G) transverse dipolar mode (1.06 eV), (H) longitudinal dipolar mode (1.50 eV), (I) hexapolar–quadrupolar mode (1.97 eV). Mode energies are indicated. Contours of the antennas are shown by black (experiment) or grey (calculations) lines. The length of the scale bars is 100 nm.

TDB mode (Figure 2C). The energy difference between the modes is below 0.1 eV. The TDA mode is apparently weaker than the TDB mode. This can be explained by the fact that the TDB mode is dark (the dipoles in both wings are antiparallel), whereas the TDA mode is bright and therefore exhibits an additional radiation damping [41]. The next peak at 1.67 eV, denoted as LD in Figure 2B, is dominated by the longitudinal dipole antibonding (LDA) mode, which features large concentration of the same-sign charge at both sides of the gap related to a large loss intensity. The peak is further contributed by the longitudinal dipole bonding (LDB) mode, observable only in the simulations. The LDB mode is bright and thus damped more than the dark LDA mode. In addition, it features accumulation of the opposite-sign charge at both sides of the gap, resulting into low loss probability in the gap area. A moderate contribution to the LD peak comes from the higher-energy hexapolar–quadrupolar modes. The third peak at 1.95 eV, denoted as HQ, is contributed by the two modes of mixed hexapolar–quadrupolar character, the hexapolar–quadrupolar bonding (HQB) mode and the hexapolar–quadrupolar antibonding (HQA) mode. Only the HQA (higher-energy mode of the HQ pair) is excited for the electron beam passing through the gap (green line in Figure 2C). These modes have been identified either as hexapolar [40, 42] or quadrupolar [11] in previous studies; their mixed character in our system is related to the wing angle of 90°. An additional high-energy mode, identified as the transverse octopolar (TO) mode, contributes to the HQ peak.

We repeat similar analysis for the diabolo antenna with nearly the same wing length $L = 150 \pm 5$ nm (differences arise due to limited accuracy of the fabrication). The antenna and its spectral response are shown in Figure 3. The experimental spectrum is composed of four peaks, which are assigned to specific modes using the energy-filtered maps of the loss intensity (Figure 3D–K) and calculated maps of the electric field and charge (see Supporting Information, Sec. S3, for details). The presence of the conductive bridge significantly influences the LD peak, which is split into LDB and LDA peaks. The LDB peak at 0.69 eV is composed of a charge transfer mode with the

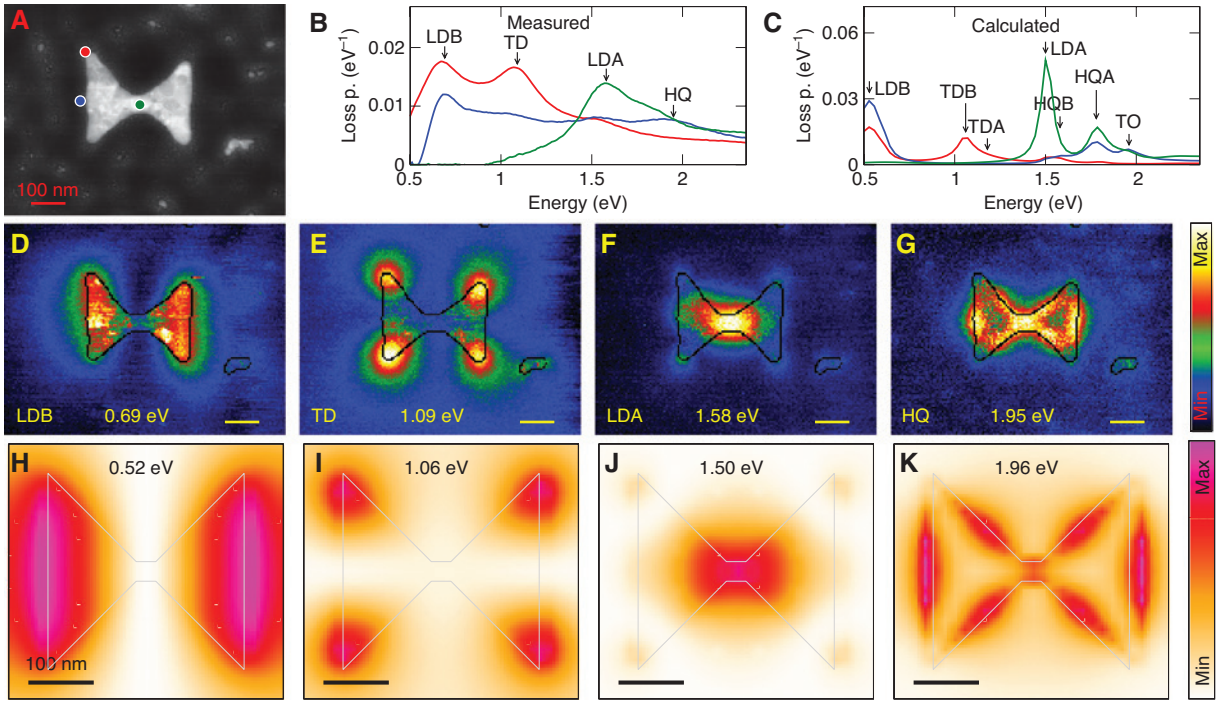

Figure 3: Diabolo antenna with the wing length $L = 150$ nm.
(A) HAADF image. (B, C) EEL spectra recorded at specific points indicated by colour spots in panel A (the spectrum displayed by a specific colour corresponds to the spot of the same colour): measured (B), calculated (C). The labels of the peaks and modes are explained in the text. (D–G) Experimental energy-filtered maps of the loss intensity for (D) longitudinal dipolar bonding mode, (E) transverse dipolar mode, (F) longitudinal dipolar antibonding mode, (G) hexapolar–quadrupolar mode. (H–K) Calculated loss intensity at the energy of (H) longitudinal dipolar bonding mode, (I) transverse dipolar mode, (J) longitudinal dipolar antibonding mode, (K) hexapolar–quadrupolar mode. Mode energies are indicated. Contours of the antennas are shown by black (experiment) or grey (calculations) lines. The length of the scale bars is 100 nm.

charge oscillating through the bridge between both wings of the diabolo antenna. Such a mode is not present in the bowtie antenna. However, the LDB mode of the bowtie is its natural counterpart. The LDB of the bowtie features a charge accumulation at the gap related with a high longitudinal electric field. When the gap is replaced with a conducting bridge, the charge flows through the bridge instead of the accumulation, forming the charge transfer mode. The transformation between both modes has been demonstrated experimentally [43]. Both modes have qualitatively identical distribution of the near field in the wings, with pronounced differences only in the bridge/gap area. For these reasons, we will label the charge transfer mode by the same label (LDB) as its counterpart in the bowtie antenna. Due to the large effective length of the antenna (the length of both the wings and bridge), the mode exhibits a huge red shift to 0.69 eV (from 1.67 eV in the bowtie) and becomes the lowest-energy mode. Similar findings hold also for other bonding modes with longitudinal charge oscillations, in particular the HQB mode.

The calculated EEL spectrum of the diabolo antenna (Figure 3C) is similar to the spectrum of the bowtie antenna (Figure 2C). Both spectra feature the modes TDB, TDA, LDA, HQA, and TO at the energies differing by less than 0.02 eV. These modes exhibit a current node within the bridge in the diabolo antennas and are therefore not very sensitive to the presence of the bridge. Only the modes LDB and HQB, which are charge transfer modes, exhibit a pronounced red shift in the diabolo antenna. The modal composition of the experimentally observed peaks is also similar to the case of the bowtie antenna; the main differences are the energy shifts of the LDB mode (which now forms the LDB peak) and the HQB mode, which now contributes more to the LDA peak and less to the HQ peak.

Figure 4A compares the energies of the modes in bowtie and diabolo antennas of different sizes (related spectra and maps are shown in Supporting Information, Sec. S2.1 and S2.2). As the experimental peaks can consist of several modes, we use the dominant modes to represent specific peaks when comparing the experiment with calculations: the LDB mode for the LDB peak, the TDB mode for the TD peak, the LDA mode for the LD/LDA peak, and the TO mode for the HQ peak. Strikingly, energies of the corresponding modes in both types of antennas are nearly identical, except for the LDB mode, which is pronouncedly red-shifted for the diabolo antenna. There is an intuitive explanation of this observation.

The modes in the dimer plasmonic antennas (such as bowtie and diabolo) can be classified as two different types. Strongly coupled modes (such as the LDB mode) extend to the area of the junction. Depending on the nature of the junction, there is either charge transfer

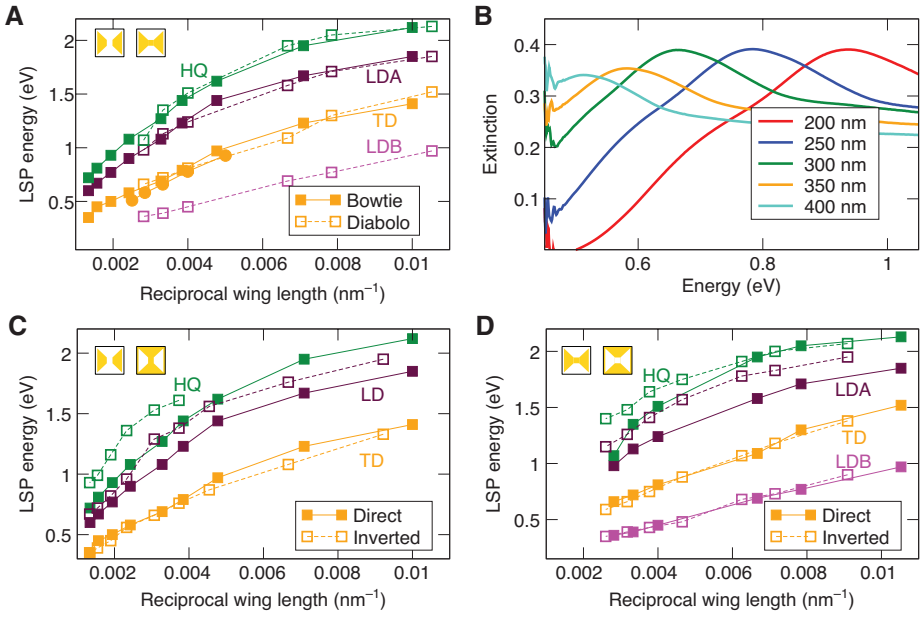

Figure 4: Energy of plasmon modes.
(A) Energies of plasmon modes in bowtie (solid lines, full symbols) and diabolo (dashed lines, empty symbols) antennas as functions of the reciprocal wing length L: longitudinal dipolar bonding (LDB) mode (magenta), transverse dipolar (TD) mode (orange), longitudinal dipolar antibonding (LDA) mode (maroon), quadrupolar–hexapolar (HQ) mode (green). Energies retrieved by EELS are shown by squares; energies from optical spectroscopy are shown by circles. (B) Optical transmission spectra of arrays of bowtie antennas for several values of the wing length. (C) Dispersion relation for the bowtie and inverted bowtie: energies of plasmon modes as functions of reciprocal wing length. (D) Dispersion relation for the diabolo and inverted diabolo: energies of plasmon modes as functions of reciprocal wing length.

through the conducting bridge or capacitive charge coupling (accumulation of opposite charges at opposite sides of the insulating gap). Properties of the strongly coupled modes pronouncedly depend on the properties of the junction. As an example, the LDB mode of the bowtie antenna exhibits an electric field hot spot at the junction, while the strongly red-shifted LDB mode of the diabolo antenna exhibits a magnetic field hot spot. Weakly coupled modes (TDB, TDA, LDA, and HQA) avoid the area of the junction, with no charge transfer or capacitive coupling, although there still might be charge accumulation (e.g. for the LDA mode). The junction affects the properties of the weakly coupled modes only slightly by modifying the dielectric environment and having some impact on the spatial distribution of the near field. However, charge oscillations are not directly influenced. The energy and near-field spatial distribution of the weakly coupled modes are thus rather insensitive to the presence or absence of the conducting bridge.

The existence of strongly and weakly coupled modes opens a prospect for the independent engineering of individual modes. The procedure is based on changing the conductivity of the antenna at the node of current oscillations of a specific mode. When a conductive connection between the two parts of the antenna is changed to a capacitive connection, the modes with the current node are only weakly modified, while the charge transfer modes are influenced significantly. On the contrary, independent antennas can be conductively connected to form new charge transfer modes.

We note that in addition to EELS we also performed optical transmission spectroscopy for arrays of bowtie antennas (Figure 4B), which exhibit only a single resolvable spectral feature corresponding to the TD mode, which couples dominantly to plane-wave excitation. Excellent agreement between the energies of the TD modes obtained by both methods supports our interpretation of the spectral features.

Experimental and calculated energies of plasmon modes agree very well to each other for both the bowtie and diabolo antennas (see Supporting Information, Sec. S1, for details). The differences up to 0.1 eV for the lowest mode and up to 0.2 eV for the higher modes are within the experimental error.

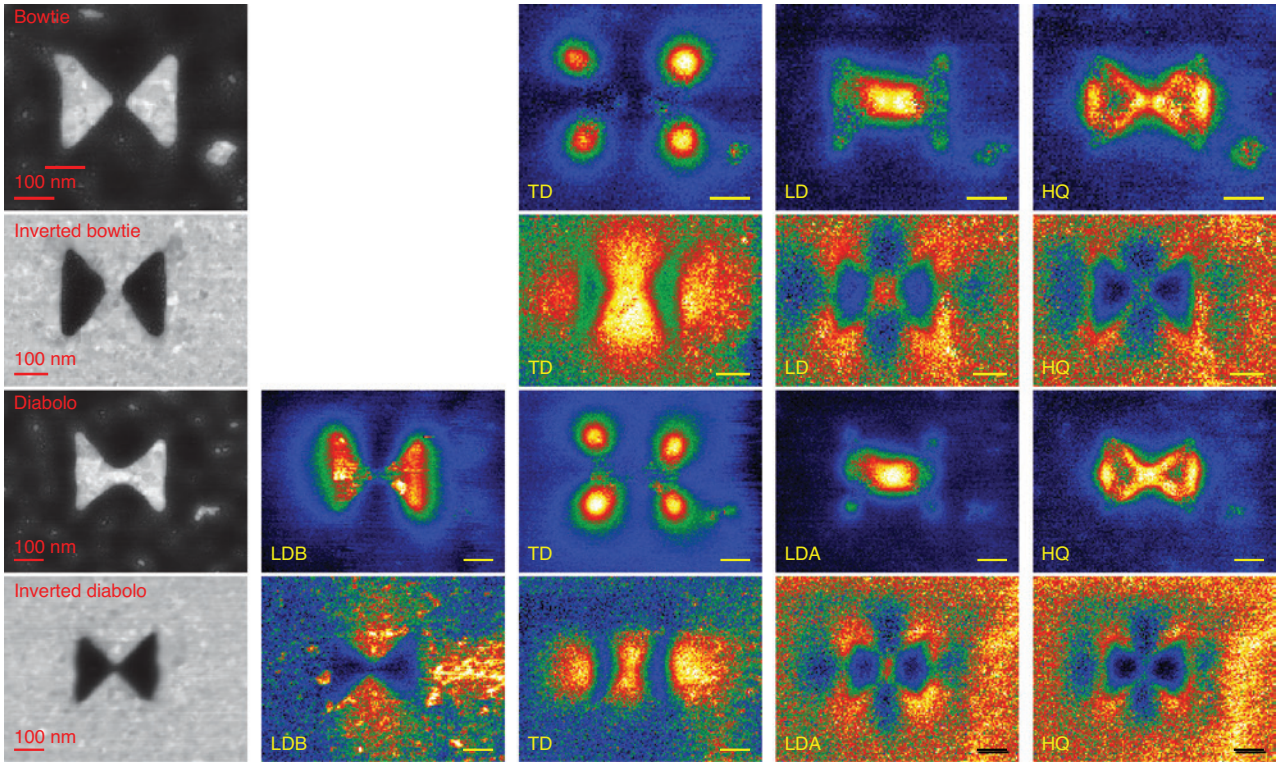

Figure 5: HAADF images of the antennas of all four types and spatial maps of the loss function at the energy corresponding to specific LSP modes: longitudinal dipolar bonding (LDB), antibonding (LDA), and, in the case of bowtie antennas, unresolved (LD), transverse dipolar (TD), and hexapolar–quadrupolar (HQ).
The energy of the modes increases from left to right. The wing length of all antennas is comparable: 140 nm (bowtie), 150 nm (diabolo), 150 nm (inverted bowtie), 140 nm (inverted diabolo). The length of the scale bars is 100 nm.

Next, we compare direct and indirect antennas related by Babinet's principle of complementarity. Inspection of the EEL spectra shows that complementary antennas exhibit resonances at similar energies but with different spatial distribution of the loss function (Figure 5). To compensate for the size differences, we plot the peak energies of the EEL spectra as functions of the reciprocal wing length in Figure 4C and D for bowtie and diabolo antennas, respectively. The interpolation between the experimentally retrieved points allows us to compare the energies of LSP modes at identical sizes of complementary antennas. We clearly observe the validity of Babinet's principle: corresponding LSP modes have identical energy (with respect to the experimental error, which is about 0.1 eV for the lowest modes and increases for the higher modes due to their overlapping in the spectra).

In Figure 5, we compare spatial maps of the loss function for specific LSP modes of all four antenna types. The size of the antennas is identical with respect to the fabrication uncertainty and varies between 140 and 150 nm (wing length). We clearly observe bowtie–diabolo duality. The modes that do not involve charge transfer through the neck of the antenna (TD, LDA, HQ) have identical spatial distribution of the loss function (and therefore of the near field). They also have similar mode energies. On the other hand, the mode LDB that includes charge transfer through the bridge of diabolo antennas has significantly different energy in bowtie antennas. Due to its spectral overlap with LDA, it was not possible to record its spatial map experimentally. The same duality holds for the direct as well as inverted bowtie–diabolo pairs.

Babinet complementarity is also clearly visible in Figure 5. The corresponding modes in direct and inverted antennas, despite having identical energy, strongly differ in the spatial distribution of the near field. The combination of Babinet's principle with the modified conductivity of junctions represents a powerful versatility in the design of plasmonic antennas with specific set of modes. The concept is exemplified by four closely related traditional nanoantennas: bowtie- and diabolo-shaped particles and apertures. We have demonstrated that all four antennas support one fixed dipolar mode (TDB) at the same energy and one dipolar mode (LDB) that can be tuned; the LDB mode can feature either electric or magnetic hot spot and can have the energy either below or above the energy of the fixed TDB mode.

Finally, we address the question how to interpret the maps of the loss intensity and what to learn about the modes. We will first consider the case of LDB mode in the diabolo antenna. Figure 6A shows schematically how

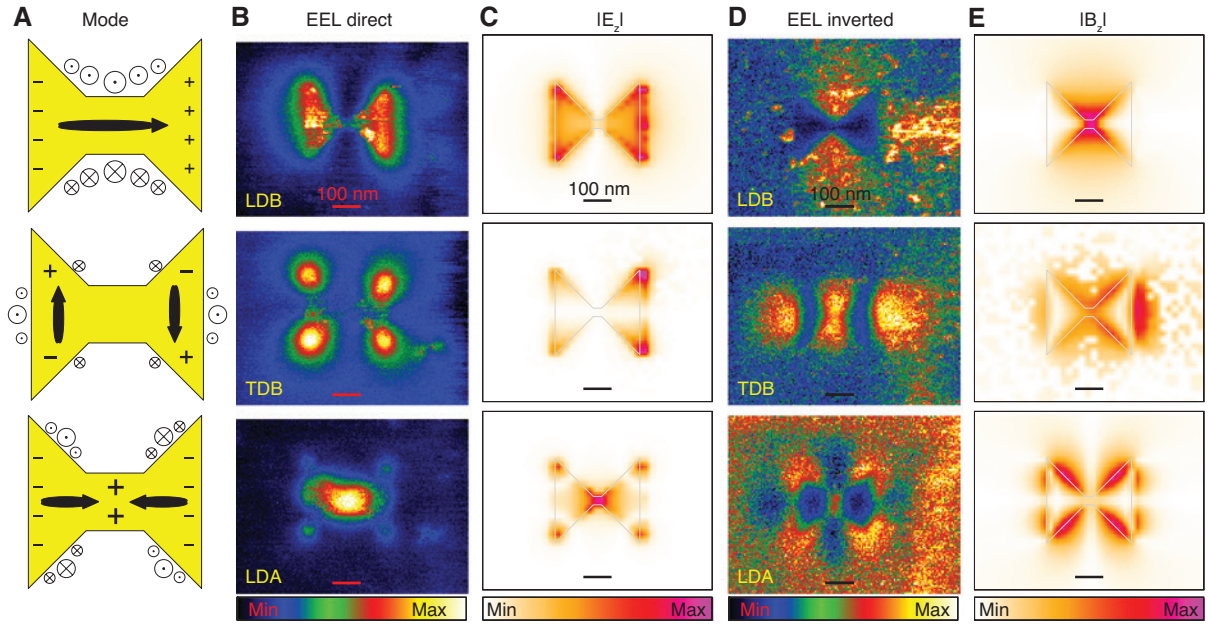

Figure 6: Experimental EEL maps and calculated fields for the LDB (1st row), TDB (2nd row), and LDA (3rd row) modes.
(A) Schematic representation of the mode in the diabolo antenna. The black arrow depicts the current with the thicker middle part representing the current antinode and the thinner border parts representing the current node. Magnetic field in the plane of the antenna is schematically represented by ⊙ (outward field) and ⊗ (inward field) symbols with the size corresponding to the magnitude of the field. The node of current corresponds to the accumulation of the charge represented by + and − symbols. (B) Experimental loss intensity distribution. (C) Calculated out-of-plane electric field. (D) Experimental loss intensity distribution for Babinet-complementary antenna (inverted diabolo). (E) Calculated out-of-plane magnetic field. The length of the scale bars is 100 nm.

current oscillates and where the charge accumulates. Loss intensity recorded by EELS is proportional to the electric field projected to the trajectory of the electron [35], i.e. out of plane of the antenna. From Gauss's law, it follows that the strongest out-of-plane electric field E_z occurs just near the areas of accumulated charge, i.e. near the edges of the diabolo. Figure 6B and C indeed show maxima of experimental loss intensity and calculated E_z at those areas. Similarly, charge node at the bridge of the diabolo related to the current antinode is manifested by the minimum of both experimental loss intensity and calculated E_z. The interpretation of the loss intensity recorded for the inverted diabolo antenna (aperture) (Figure 6D) is less straightforward as the current distribution of the related plasmon mode is not trivial. Instead, we will relate the loss intensity distribution of inverted antenna to the current distribution of the direct antenna. Loss intensity in the inverted antenna is proportional to the out-of-plane electric field, which is according to Babinet's principle proportional to the out-of-plane component of the magnetic field in the direct antenna. Indeed, magnetic field in the direct antenna according to Ampère's law circulates around the electric current with the maxima around the antinodes of the current (Figure 6A). Both the experimental loss intensity in the inverted antenna (Figure 6D) and the calculated out-of-plane magnetic field in the direct antenna (Figure 6E) exhibit maxima in the hot spot around the current's antinode inside the bridge of the diabolo. In this way, EELS in combination with Babinet's principle can be used for indirect magnetic field imaging. It is particularly interesting that EELS, known to be blind to electric hot spots in the standard configuration [38], is capable of imaging the magnetic hot spot. This fact is related to the vectorial character of the magnetic field in the hot spot with nonzero out-of-plane component.

Similar considerations can be repeated for TDB mode and LDA mode or for bowtie antenna. Schemes of the charge oscillations together with the calculated electric and magnetic field distribution are shown in the second and third lines of Figure 6 for the TDB and LDA modes, respectively. As in the case of LDB mode, bright spots in the loss intensity of direct antennas correspond to the strong out-of-plane component of the electric field related to the accumulated charge, and bright spots in the loss intensity of the Babinet-complementary antennas (apertures) correspond to the strong out-of-plane component of the magnetic field that circulates around antinodes of the current density.

4 Conclusion

We have demonstrated a unique approach of independent engineering of individual LSP modes in composite plasmonic antennas based on varying the coupling between the components from capacitive to conductive. Taking bowtie and diabolo antennas as an example, we have shown that the longitudinal dipolar mode can be significantly modified (including switching between electric and magnetic hot spot) without affecting the higher-order modes. In combination with Babinet's principle allowing engineering independently spectral and spatial properties of LSP modes, this represents a powerful tool for tailoring the properties of LSP modes for the phenomena and applications including Fano resonances, directional scattering, or enhanced luminescence.

Acknowledgement: We acknowledge the support by the Czech Science Foundation (grant 17-25799S, Funder Id: http://dx.doi.org/10.13039/501100001824); European Union's Horizon 2020 (project SINNCE, no. 810626, Funder Id: http://dx.doi.org/10.13039/100010684); Ministry of Education, Youth and Sports of the Czech Republic (projects CEITEC 2020, no. LQ1601, Funder Id: http://dx.doi.org/10.13039/501100001823; and CEITEC Nano RI, no. LM2015041, Funder Id: http://dx.doi.org/10.13039/501100001823); and Brno University of Technology (grant FSI/STI-J-18-5225).

References

[1] Novotny L, van Hulst N. Antennas for light. Nat Photonics 2011;5:83–90.
[2] Klein MW, Enkrich C, Wegener M, Linden S. Second-harmonic generation from magnetic metamaterials. Science 2006;313:502–4.
[3] Feth N, Linden S, Klein MW, et al. Second-harmonic generation from split-ring resonators on a GaAs substrate. Opt Lett 2008;33:1975–7.
[4] Atie EM, Xie Z, El Eter A, et al. Remote optical sensing on the nanometer scale with a bowtie aperture nano-antenna on a fiber tip of scanning near-field optical microscopy. Appl Phys Lett 2015;106:151104.
[5] Inkhabwala A, Yu Z, Fan S, Avlasevich Y, Müllen Y, Moerner WE. Large single-molecule fluorescence enhancements produced by a bowtie nanoantenna. Nat Photonics 2009; 3:654–7.
[6] Yu N, Capasso F. Flat optics with designer metasurfaces. Nat Mater 2014;13:139–50.
[7] Nordlander P, Oubre C, Prodan E, Li K, Stockman MI. Plasmon hybridization in nanoparticle dimers. Nano Lett 2004;4: 899–903.
[8] Davis TJ, Gómez DE, Vernon KC. Simple model for the hybridization of surface plasmon resonances in metallic nanoparticles. Nano Lett 2010;10:2618–25.
[9] Brandl DW, Mirin NA, Nordlander P. Plasmon modes of nanosphere trimers and quadrumers. J Phys Chem B 2006;110:12302–10.

[10] Koh AL, Fernández-Domínguez AI, McComb DW, Maier SA, Yang JKW. High-resolution mapping of electron-beam-excited plasmon modes in lithographically defined gold nanostructures. Nano Lett 2011;11:1323–30.
[11] Duan H, Fernández-Domínguez AI, Bosman M, Maier SA, Yang JKW. Nanoplasmonics: classical down to the nanometer scale. Nano Lett 2012;12:1683–9.
[12] Born M, Wolf E, Bhatia A. Principles of Optics: Electromagnetic theory of propagation, interference and diffraction of light. Cambridge, United Kingdom: Cambridge University Press, 1999.
[13] Falcone F, Lopetegi T, Laso MAG, et al. Babinet principle applied to the design of metasurfaces and metamaterials. Phys Rev Lett 2004;93:197401.
[14] Zentgraf T, Meyrath TP, Seidel A, et al. Babinet's principle for optical frequency metamaterials and nanoantennas. Phys Rev B 2007;76:033407.
[15] Hentschel M, Weiss T, Bagheri S, Giessen H. Babinet to the half: coupling of solid and inverse plasmonic structures. Nano Lett 2013;13:4428–33.
[16] Bitzer A, Ortner A, Merbold H, Feurer T, Walther M. Terahertz near-field microscopy of complementary planar metamaterials: Babinet's principle. Opt Express 2011;19:2537–45.
[17] Rossouw D, Botton GA. Resonant optical excitations in complementary plasmonic nanostructures. Opt Express 2012;20:6968–73.
[18] Mizobata H, Ueno K, Misawa H, Okamoto H, Imura K. Near-field spectroscopic properties of complementary gold nanostructures: applicability of Babinet's principle in the optical region. Opt Express 2017;25:5279–89.
[19] von Cube F, Irsen S, Niegemann J, et al. Spatio-spectral characterization of photonic meta-atoms with electron energy-loss spectroscopy. Opt Mater Express 2011;1:1009–18.
[20] Horák M, Křápek V, Hrtoň M, et al. Limits of Babinet's principle for solid and hollow plasmonic antennas. Sci Rep 2019;9:4004.
[21] Chen H-T, O'Hara JF, Taylor AJ, et al. Complementary planar terahertz metamaterials. Opt Express 2007;15:1084.
[22] Hrtoň M, Konečná A, Horák M, Šikola T, Křápek V. arXiv e-prints, arXiv:1904.01397 2019.
[23] Chen Y, Chen Y, Chu J, Xu X. Bridged bowtie aperture antenna for producing an electromagnetic hot spot. ACS Photonics 2017;4:567–75.
[24] Ögüt B, Vogelgesang R, Sigle W, Talebi N, Koch CT, van Aken PA. Hybridized metal slit eigenmodes as an illustration of Babinet's Principle. ACS Nano 2011;5:6701–6.
[25] Itoh T, Yamamoto YS, Ozaki Y. Plasmon-enhanced spectroscopy of absorption and spontaneous emissions explained using cavity quantum optics. Chem Soc Rev 2017;46:3904–21.
[26] Vercruysse D, Zheng X, Sonnefraud Y, et al. Directional fluorescence emission by individual V-antennas explained by mode expansion. ACS Nano 2014;8:8232–41.
[27] Zhang J, ElKabbash M, Wei R, Singh SC, Lam B, Guo C. Plasmonic metasurfaces with 42.3% transmission efficiency in the visible. Light Sci Appl 2019;8:53.
[28] Kerker M, Wang D-S, Giles CL. Electromagnetic scattering by magnetic spheres. J Opt Soc Am 1983;73:765–7.
[29] Liu W, Kivshar YS. Generalized Kerker effects in nanophotonics and meta-optics [Invited]. Opt Express 2018;26:13085–105.
[30] Verellen N, Sonnefraud Y, Sobhani H, et al. Fano resonances in individual coherent plasmonic nanocavities. Nano Lett 2009;9:1663–7.
[31] Zhang S, Genov DA, Wang Y, Liu M, Zhang X. Plasmon-induced transparency in metamaterials. Phys Rev Lett 2008;101:047401.
[32] Hentschel M, Dregely D, Vogelgesang R, Giessen H, Liu N. Plasmonic oligomers: the role of individual particles in collective behavior. ACS Nano 2011;5:2042–50.
[33] Křápek V, Koh AL, Břínek L, et al. Spatially resolved electron energy loss spectroscopy of crescent-shaped plasmonic antennas. Opt Express 2015;23:11855–67.
[34] Horák M, Bukvišová K, Švarc V, Jaskowiec J, Křápek V, Šikola T. Comparative study of plasmonic antennas fabricated by electron beam and focused ion beam lithography. Sci Rep 2018;8:9640.
[35] García de Abajo FJ. Optical excitations in electron microscopy. Rev Mod Phys 2010;82:209–75.
[36] García de Abajo FJ, Kociak M. Probing the photonic local density of states with electron energy loss spectroscopy. Phys Rev Lett 2008;100:106804.
[37] Kociak M, Stéphan O. Mapping plasmons at the nanometer scale in an electron microscope. Chem Soc Rev 2014;43:3865–83.
[38] Hohenester U, Ditlbacher H, Krenn JR. Electron-energy-loss spectra of plasmonic nanoparticles. Phys Rev Lett 2009;103:106801.
[39] Johnson PB, Christy RW. Optical constants of the noble metals. Phys Rev B 1972;6:4370.
[40] Schmidt FP, Ditlbacher H, Hofer F, Krenn JR, Hohenester U. Morphing a plasmonic nanodisk into a nanotriangle. Nano Lett 2014;14:4810–5.
[41] Kats MA, Yu N, Genevet P, Gaburro Z, Capasso F. Effect of radiation damping on the spectral response of plasmonic components. Opt Express 2011;19:21748–53.
[42] Myroshnychenko V, Nishio N, García de Abajo FJ, Förstner J, Yamamoto N. Unveiling and imaging degenerate states in plasmonic nanoparticles with nanometer resolution. ACS Nano 2018;12:8436–46.
[43] Schnell M, García-Etxarri A, Huber AJ, Crozier K, Aizpurua J, Hillenbrand R. Controlling the near-field oscillations of loaded plasmonic nanoantennas. Nat Photonics 2009;3:287–91.

Supplementary Material: The online version of this article offers supplementary material (https://doi.org/10.1515/nanoph-2019-0326).